ACS POLYMERS Au
AN OPEN ACCESS JOURNAL OF THE AMERICAN CHEMICAL SOCIETY

pubs.acs.org/polymerau

Article

Directly Probing the Fracture Behavior of Ultrathin Polymeric Films

Song Zhang, Masato Koizumi, Zhiqiang Cao, Keyou S. Mao, Zhiyuan Qian, Luke A. Galuska, Lihua Jin,* and Xiaodan Gu*

Cite This: *ACS Polym. Au* 2021, 1, 16–29

Read Online

ACCESS | Metrics & More | Article Recommendations | Supporting Information

ABSTRACT: Understanding fracture mechanics of ultrathin polymeric films is crucial for modern technologies, including semiconductor and coating industries. However, up to now, the fracture behavior of sub-100 nm polymeric thin films is rarely explored due to challenges in handling samples and limited testing methods available. In this work, we report a new testing methodology that can not only visualize the evolution of the local stress distribution through wrinkling patterns and crack propagation during the deformation of ultrathin films but also directly measure their fracture energies. Using ultrathin polystyrene films as a model system, we both experimentally and computationally investigate the effect of the film thickness and molecular weight on their fracture behavior, both of which show a ductile-to-brittle transition. Furthermore, we demonstrate the broad applicability of this testing method in semicrystalline semiconducting polymers. We anticipate our methodology described here could provide new ways of studying the fracture behavior of ultrathin films under confinement.

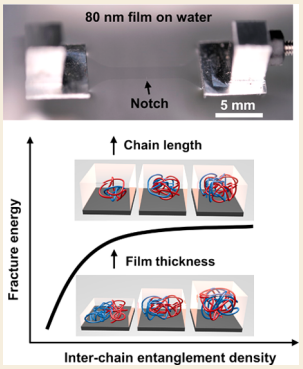

KEYWORDS: *fracture, fracture energy, thin film, confinement, stretchable electronics*

1. INTRODUCTION

Recent technology development has brought wide applications of ultrathin films (<100 nm) into our daily life, such as optical coatings, filtration membranes, and semiconducting devices.[1−9] Characterizing and understanding the mechanical properties of ultrathin films is critical for their end applications but extremely challenging because of their delicate nature. Traditionally, an underlying solid substrate is required to support thin films in mechanical tests.[10,11] However, this is unfavorable because unknown film−substrate interactions might obscure the intrinsic properties of thin films.[12−16] Recent reports on pseudo-free-standing tensile tests address this limitation through measuring ultrathin films afloat on water, and their mechanical properties, like elastic modulus and crack-onset strain, have been successfully measured.[17−22]

Nevertheless, measuring a fracture energy, an intrinsic material property that quantifies the capability of a material to resist propagation of a pre-existing crack, is missing in the literature for pristine ultrathin films despite its decisive role in determining the failure behavior of bulk polymer samples.[23,24] In the previous works, microprojectile impact tests have been applied to obtain the energy absorption of ultrathin films under high-strain-rate deformation,[25−27] and four-point bending tests and double-cantilever beam tests are used to measure the adhesive/cohesive fracture energies for multilayer thin-film systems or binary blends.[28−31] However, the influence of thermal energy dissipation and the substrate can obscure the quantitative measurement. The direct characterization of the fracture energies of ultrathin films can provide the most fundamental material−property relationships and guidelines for material selection and product development.

Here, we present the first direct measurement of the fracture energy of an ultrathin glassy polymer film down to a thickness of 26 nm through a pseudo-free-standing tensile tester with the Begley−Landes method and pure shear method. Using polystyrene (PS) as a model material system, we determine by experiments and finite element simulations the stress distribution near a crack tip, which is characterized by wrinkling patterns perpendicular to the strain direction near the crack and propagating downstream as the crack extends. The experimentally and computationally characterized fracture energy is shown to undergo a significant reduction, featured by a ductile-to-brittle transition, when the molecular weight is decreased below a critical value, which is attributed to the loss of interchain entanglements in short polymer chains.[32−34] Similarly, due to the loss of interchain entanglements under nanoscale confinement, the fracture energy of PS also reduces as the film thickness approaches the end-to-end distance (R_{ee}) of the polymer chains.[12,35,36] To highlight the broad applicability of this methodology, the fracture energies of several conjugated polymers, poly{[*N*,*N*′-bis(2-hexyldecyl)-naphthalene-1,4,5,8-bis(dicarboximide)-2,6-diyl]-*alt*-2,5-thio-

Received: April 1, 2021
Published: June 22, 2021

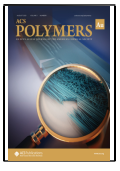

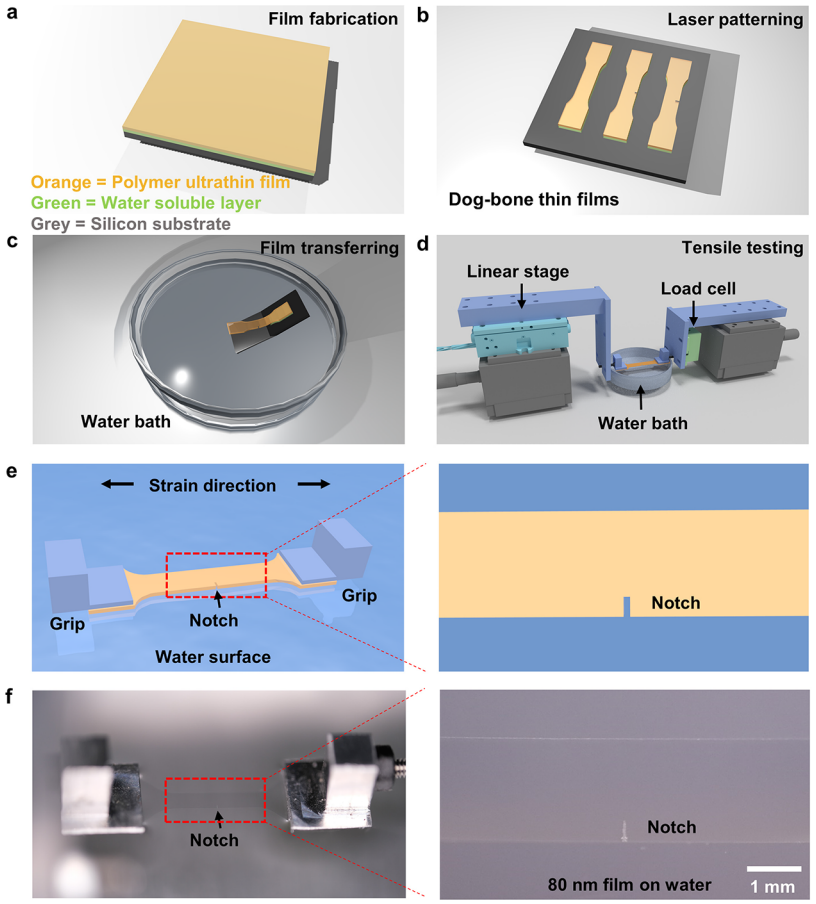

Figure 1. Demonstration of the thin-film fracture energy test based on an 80 nm thick polystyrene film with a molecular weight of 173 kg/mol. (a–e) 3D schematics showing the procedures of fabricating and conducting the fracture test to the thin film. (a) Double-layer thin film composed of a water-soluble layer and a polystyrene layer cast on a silicon wafer. (b) Laser patterning of dog-bone-shaped films with varied notch lengths. (c) Ultrathin films floating on the water surface by releasing the water-soluble layer. (d) Tensile testing of thin-film mechanics through a pseudo-free-standing tensile tester. (e) Uniaxial tensile testing of a notched ultrathin film on the water surface with grips on both ends. (f) Optical images showing an 80 nm polystyrene ultrathin film with a notch size of 0.4 mm floating on water. The gauge length and width are 8 and 2 mm, respectively.

phene} (PNDI(2HD)T) and poly(3-hexylthiophene) (P3HT) are measured. Our technique provides a general platform for fracture energy measurement of ultrathin polymeric films and is applicable to metals and emerging 2D materials, which are vital for understanding their failure behavior for energy and healthcare applications.

2. RESULTS AND DISCUSSION

2.1. Fabrication of Ultrathin Films

In this work, we first introduce a new technique to directly measure the fracture energies of ultrathin films (e.g., <100 nm) supported on a water surface. We use a classic glassy polymer, PS, with a number-averaged molecular weight (M_n) of 173 kg/mol, as a model system to demonstrate the capability of this methodology (Figure 1). A water-soluble layer of poly(styrenesulfonate) (PSS) was spin-coated on the top of a silicon wafer, followed by coating a layer of 80 nm PS ultrathin film to form a bilayer composite (Figure 1a). Next, the film was laser-patterned into a dog-bone shape with a gauge width of 2 mm and length of 8 mm, where a single-edge notch with a length c of 0, 0.2, 0.4, 0.6, and 0.8 mm was also introduced through laser etching (Figure 1b and Figure S1). Upon dipping the edge of the bilayer film in water, the PSS layer was dissolved, and the PS layer was released on the water surface (Figure 1c). Later, the PS film was transferred and mounted to two aluminum grips, one connected to a linear stage and the other attached to a load cell (Figure 1d). A similar transfer method was described in detail in our previous publications.[18,37−39] After the transfer, the afloat film is ready for a mechanical test. Both a schematic and an optical microscope image of a notched film floating on the water surface are shown in Figure 1e,f, respectively.

2.2. Visualization of Stress Distribution

During the stretching process, the film first experiences elastic deformation at a small external displacement; correspondingly, the film surface stays flat when the notch opened along the strain direction (Movie S1). Next, periodical wrinkling patterns aligning parallel to the strain direction are observed around the notch due to the gradual increase of the compressive stress in the vicinity of the notch tip (Figure 2a,b).[40] Figure 2c shows optical images of notched PS ultrathin films with a thickness of 80 nm and different notch lengths at different displacements. As the displacement increases, the wrinkling pattern slowly builds up near the notch tip and propagates outward, indicating that a larger region of the film undergoes high compressive stress. The wrinkles pack more densely in the area closer to the tip, indicating higher stress. For samples with a

https://doi.org/10.1021/acspolymersau.1c00005
ACS Polym. Au 2021, 1, 16−29

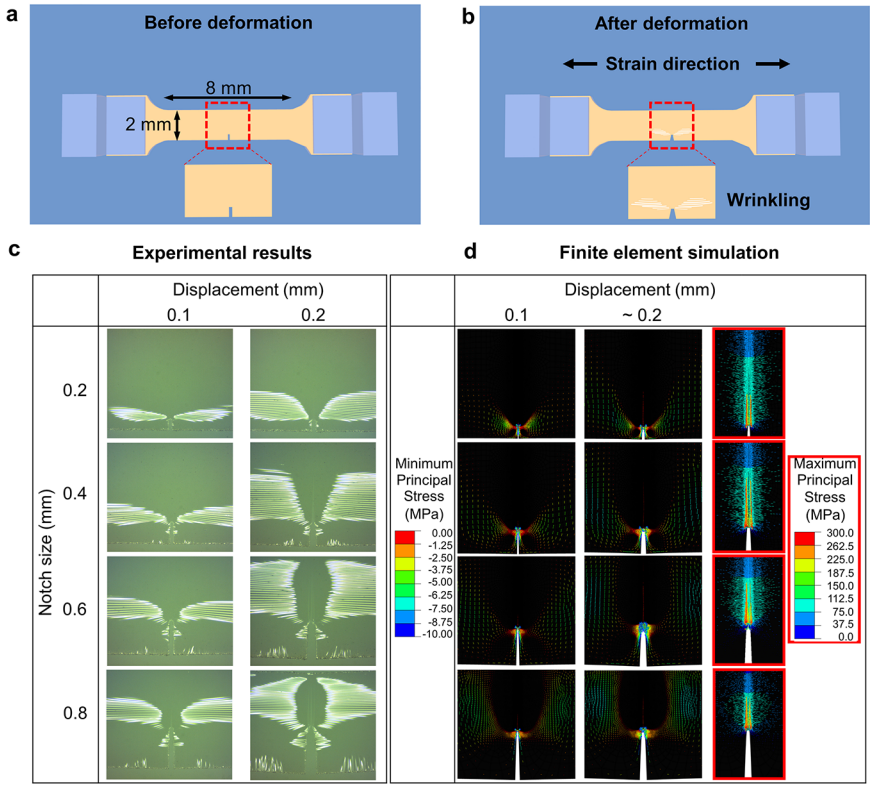

Figure 2. Deformation of notched polystyrene thin films under tensile strain. (a,b) 3D schematics showing a dog-bone sample with a notch (a) before and (b) after deformation. When the deformation is large enough, wrinkles show up near the notch. (c) Optical images of thin films with notches of various sizes being uniaxially deformed to different displacements. (d) Finite element simulation results of minimum principal stress distribution in notched polystyrene thin films of various notch sizes (shared with (c)) subjected to different deformations. The orientation of the minimum principal stress indicates the direction of the wrinkling patterns. Since some films have catastrophically failed at the displacement 0.2 mm, the stress distributions are shown at smaller displacements (0.19, 0.16, and 0.14 mm for samples with a notch size of 0.4, 0.6, and 0.8 mm, respectively). Images with red frames represent the corresponding maximum principal stress distributions, which show high tensile stress at the crack tip.

longer initial notch, the number of wrinkles at a given displacement is higher, owing to the reduced cross-sectional area and higher stress at the notch tip. When the stress around the tip reaches a critical value, the film begins yielding plastically. As the crack starts to propagate, plastic deformation dominates the vicinity of the notch tip, indicated by the expanding white triangle regions near the tip, known as the shear deformation zone (SDZ) (Figure 2c and Figure S2). During the crack propagation, the original wrinkles disappear while new ones show up along with the propagation of the SDZ due to the redistribution of the stress field. To demonstrate the evolution of the stress field in the film as the external displacement increases, we also conducted finite element simulations for PS films with a precrack of various lengths, same as the experiments, subjected to external displacement loading under the plane stress condition using ABAQUS. The PS film was modeled as an elasto-plastic material using a J_2 flow theory and isotropic hardening. Previous literature has demonstrated that the postyielding stress−strain relation of glassy thermoplastics shows strain hardening and follows the Gaussian chain statistics in accordance with the rubber elasticity.[41] In this study, considering the stress concentration in the vicinity of a crack tip, we substituted the Gent model for the Gaussian equation to capture the strain stiffening effect under large deformation:

$$\sigma = \sigma_Y + \left(\frac{J_m G_p}{J_m - \lambda^2 - 2/\lambda}\right)\left(\lambda^2 - \frac{1}{\lambda}\right) \quad (1)$$

where σ is the true von Mises stress, σ_Y is the yield stress, λ is the equivalent stretch defined as $\lambda = \exp(\epsilon_p)$ with ϵ_p being the true equivalent plastic strain, and G_p is the strain-hardening modulus. The parameter J_m governs the strain stiffening effect by setting the stretching limit, and when $\lambda^2 - 2/\lambda$ reaches J_m, stress σ approaches infinity. We determined the parameters from our measurements or the literature: σ_Y = 84 MPa (Figure 5a and Figure S3c), G_p = 15 MPa, J_m = 200, along with Young's modulus E = 3.01 GPa and Poisson's ratio ν = 0.34 for the linearly elastic regime (see the Methods section).[42] A layer of cohesive elements modeled by a bilinear traction−separation law was inserted in front of the notch to allow propagation of the notch under the assumption of a pure mode I crack (see the Methods section and Figures S3a,b and S15c). Here, we set the following parameters: the intrinsic fracture energy Γ_0 = 100 J/m^2, maximum cohesive stress σ_c = 300 MPa, and the interfacial stiffness of the cohesive elements E_{ts} = 78750 GPa (see the discussion about Figure 5 and Methods section for additional details).

As a result, stress concentrates at the crack tip, dominated by plasticity (Figure 2d and Figure S2b). Figure 2d shows the symbol plot of the minimum principal stress, where the direction of a line represents the orientation of the minimum principal stress. The negative value of the minimum principal

https://doi.org/10.1021/acspolymersau.1c00005
ACS Polym. Au 2021, 1, 16−29

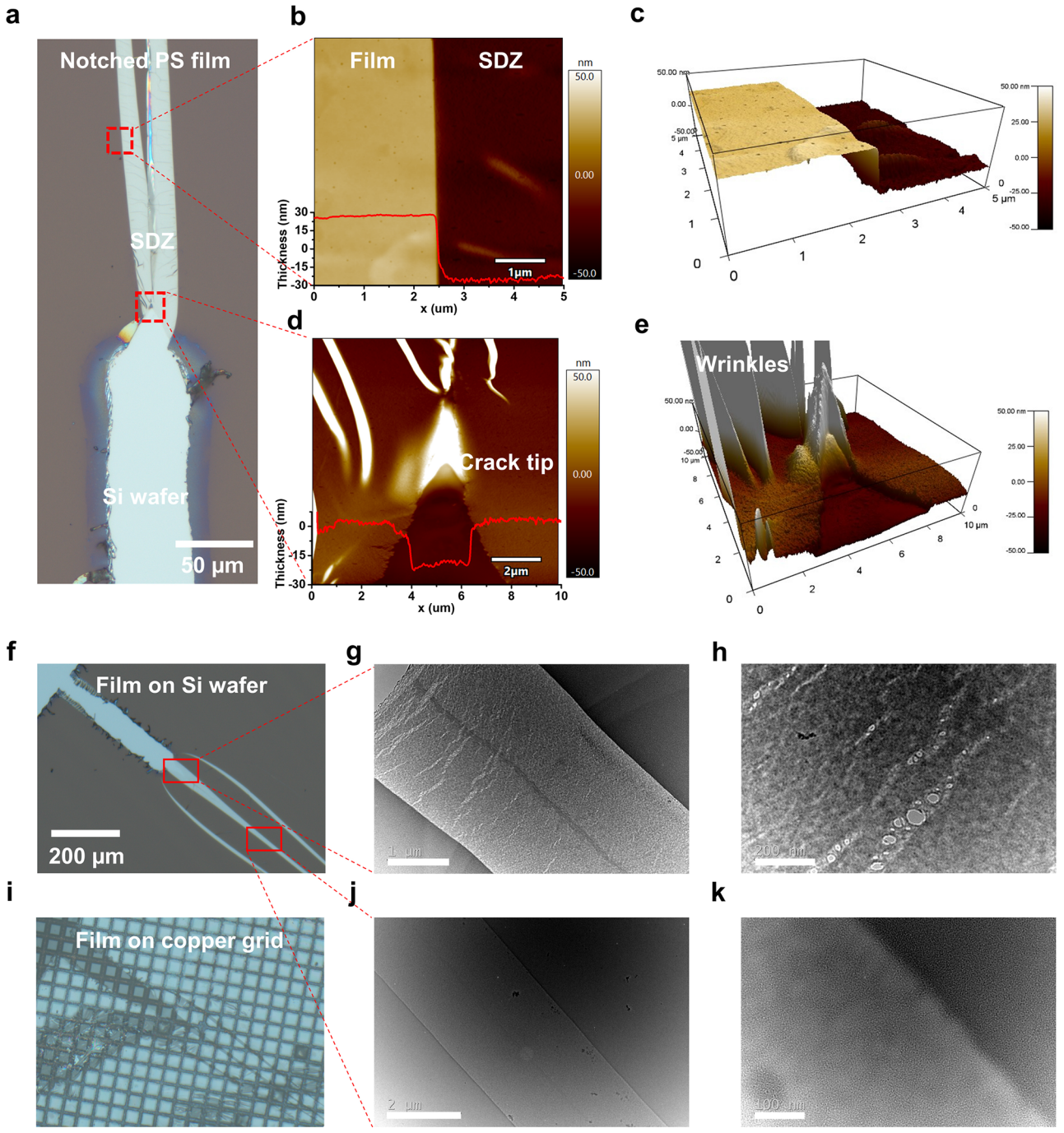

Figure 3. Images for shear deformation zone at the notch tip. (a) Optical image of the crack tip for a notched film sitting on a silicon wafer (0.4 mm notch size and 0.2 mm displacement). (b) AFM 2D and (c) 3D height images showing the boundary between a shear deformation zone (SDZ) and the rest of the film. 1D line cut is overlaid to show the film thickness along the sample. (d) AFM 2D and (e) 3D height images of the notch tip. 1D line cut is overlaid to show the film thickness along the sample. (f) Optical images for notched film on Si wafer and (i) copper grid. (g,h) TEM images for SDZ at the notch tip and (j,k) far from the notch tip. Scale bars: (g) 1 μm, (h) 200 nm, (j) 2 μm, and (k) 100 nm.

stress indicates wrinkling patterns should align perpendicular to it, parallel to the strain direction, similar to the experimental observation. As the external displacement increases, the compressive stress increases, and the wrinkling patterns expand. Since some films have catastrophically failed before the displacement 0.2 mm in our simulations, their stress distributions are shown at smaller displacements, that is, 0.19, 0.16, and 0.14 mm for samples with a notch size of 0.4, 0.6, and 0.8 mm, respectively. As the initial notch length increases, the wrinkling regions enlarge and align more in the crack direction. High tensile stress exists at the notch tip in the perpendicular direction, represented by the maximum principal logarithmic stress, implying the formation of the SDZ at similar locations to the experiments (Figure 2d).

To better visualize the local deformation behavior around the notch, both optical microscopy and atomic force microscopy (AFM) were applied to investigate the thin-film morphology near the crack tip. The ultrathin PS film with a notch size of 0.4 mm was strained to 2.5% externally (0.2 mm displacement) and then picked up from the water by a silicon

https://doi.org/10.1021/acspolymersau.1c00005
ACS Polym. Au 2021, 1, 16−29

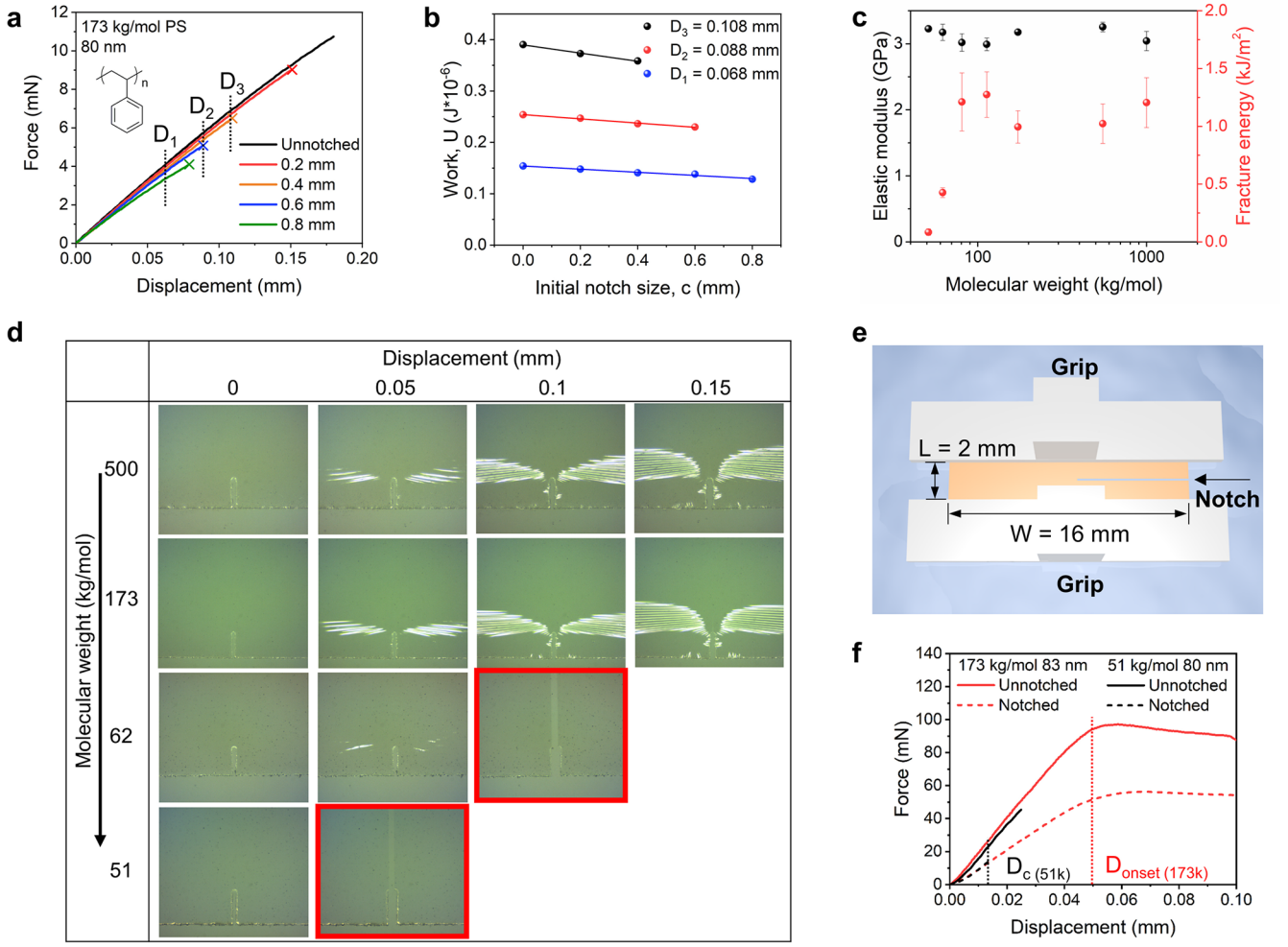

Figure 4. Fracture energy measurements of PS ultrathin films through experimental methods. (a–d) Begley–Landes method. (a) Force–displacement curves for various notch lengths of 173 kg/mol PS thin films. The end points of the curves represent the beginning of crack propagation. (b) Total work done to the samples, calculated using the area underneath the force–displacement curves at given displacement values, is plotted as a function of the initial notch size. (c) Elastic modulus (black) and fracture energy (red) for 80 nm PS ultrathin films with different molecular weights. (d) Optical images of an 80 nm PS film with 0.4 mm notch length and various molecular weights at different displacements. Images with red frames represent fractured films. (e,f) Pure shear test method. (e) Schematics of the test setup with a rectangular notched sample attached to grips on two ends. (f) Force–displacement curves for unnotched and notched PS films with the molecular weight of 173 and 51 kg/mol. D_c represents the critical displacement of the 51 kg/mol PS; D_{onset} represents the onset of notch propagation for the 173 kg/mol PS.

substrate (Figure 3 and Figure S4). It is observed that, as the notch propagates, the nearby PS film undergoes substantial plastic deformation, which induces chain reorientation, chain disentanglement, and chain scission. In particular, the local chain disentanglement behavior corresponds to the formation of SDZs at the notch tip, seen as the white band-like regions around the crack tip (Figure 3a). AFM height images of the SDZ indicate that its thickness is 25 nm, which means a 70% reduction in its original thickness of 80 nm, suggesting a significant amount of plastic deformation in the SDZ (Figure 3b–e). Similar observations have also been reported elsewhere.[43] To further investigate the morphology of SDZ, transmission electron microscopy (TEM) experiments were performed (Figure 3f–k). At SDZ close to the notch tip, strip-like voids were seen during deformation (Figure 3g,h), which is similar to previously reported "2D crazes" by Bay et al.[20] However, no clear crazes showed up in the SDZ far from the notch (Figure 3j,k).

2.3. Fracture Energy Measurement with Begley–Landes Method

To further measure the fracture energy of the ultrathin PS films, the dependence of force F on displacement D was recorded and plotted in Figure 4a. The unnotched sample curve is shown in black, where only a portion of the full curve is shown for better comparison. The cross on the end of each curve represents the onset of crack propagation, as visualized through a high-resolution camera. The total work done to the sample, $U(D)$, can be calculated from the area underneath the force–displacement curve for various notch sizes c and later plotted as a function of c (Figure 4b). The fracture energy was calculated based on the following equation:

$$G_c = \frac{1}{t}\frac{dU}{dc}\bigg|_D \tag{2}$$

where t is the film thickness, D represents the selected displacement that is close to the onset of crack propagation (i.e., D_1, D_2, and D_3).[44,45] As a result, the fracture energy of an

https://doi.org/10.1021/acspolymersau.1c00005
ACS Polym. Au 2021, 1, 16–29

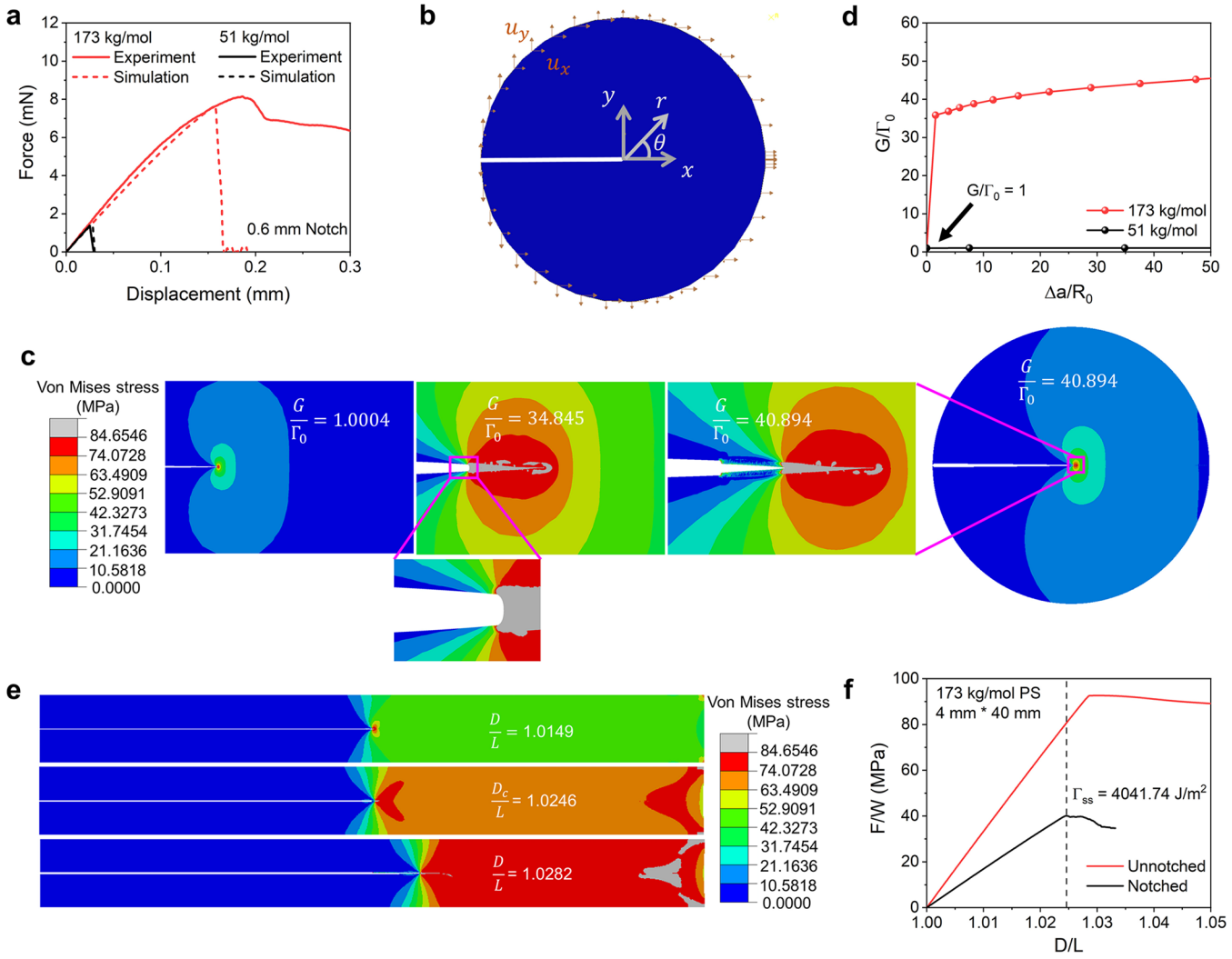

Figure 5. Fracture energy measurements of PS ultrathin films through finite element analysis. (a) Comparison of force−displacement curves between experimental and simulation results for 173 and 51 kg/mol PS dog-bone samples with a 0.6 mm notch. The 173 kg/mol PS is modeled as an elasto-plastic material, whereas the 51 kg/mol PS is modeled as an elastic material. (b−d) Fracture simulations results based on the K-field zone method. (b) Schematic of a K-field zone subjected to applied displacement loading. (c) Zoom-in view of the evolution of the plastic zone for a 173 kg/mol PS film; that is, as the external loading increases, the plastic zone expands and the crack propagates. The gray region indicates the plastic zone with the von Mises stress beyond the yield stress. The film exhibits ductile fracture, indicated by the blunting of the crack tip. (d) Crack growth resistance curves for the 173 and 51 kg/mol PS. The fracture energy for the 51 kg/mol PS remains a constant, whereas the one for the 173 kg/mol PS significantly increases with the crack extension to more than 40 times of the intrinsic fracture energy due to plastic dissipation. (e,f) Fracture simulations results based on the pure shear method. (e) Evolution of the plastic zone and crack propagation as the external displacement increases in a pure shear simulation model for the 173 kg/mol PS. (f) Relations between the normalized force F/W and normalized displacement D/L for the notched and unnotched 173 kg/mol PS in the pure shear simulations.

80 nm thick 173 kg/mol PS film was determined to be 995 J/m^2, which was within the range from 200 to 1700 J/m^2, as reported by various studies on bulk PS samples.[23,46] This wide range of reported values in the literature was ascribed to different sample preparation and processing methods, as well as morphology change during crack growth.[47,48] Previous works by Bay and Crosby and our group have identified the effect of water in increasing craze stability and retarding strain localization in ultrathin films, which lead to a higher crack onset strain.[21,22] In fracture tests, the water underneath the notched samples is also expected to influence the energy release rate, that is, the driving force for the crack propagation, due to its surface energy, which is not accounted for in our measurement. However, since the surface energy of water is much lower than the fracture energy of the film, the effect of water on the measured fracture energy is negligible. This warrants future tests of fracture energy for fully free-standing films.

2.4. Molecular Weight Effect on Fracture Energy

Next, we examined the role of plastic deformation in resisting crack propagation by varying the molecular weight. Previous studies on bulk PS have shown a ductile-to-brittle transition with decreasing molecular weight, indicating molecular-weight-dependent fracture energy.[34,49] A similar phenomenon has also been widely observed in other polymers such as poly(methyl methacrylate) (PMMA) and polyimide.[33,50−52] Microprojectile impact tests performed on free-standing PS thin films show decreased impact energy as the chain entanglement decreases.[25] Here, we also tested PS ultrathin films with various molecular weights (51, 62, 81, 113, 500, 1000 kg/mol)

https://doi.org/10.1021/acspolymersau.1c00005
ACS Polym. Au 2021, 1, 16−29

at a similar film thickness of around 80 nm (Figure 4c,d and Figures S5−S12). Their corresponding elastic moduli and fracture energies are plotted in Figure 4c and summarized in Table S1. While ductile behavior is found in 173 kg/mol PS films, 51 kg/mol PS films show brittle failure. The elastic modulus shows no apparent dependence on the molecular weight since the lowest molecular weight tested here is well above the entanglement molecular weight of PS (M_e = 18 kg/mol) (Figure S13a).[16,53] Similarly, their bulk glass transition temperature T_g is independent of the molecular weight in the range studied here (Figure S13b).[54] In contrast, the fracture energy drops significantly at below 82 kg/mol, that is, the fracture energy of 62 and 51 kg/mol PS is 426 and 84 J/m^2, which are 68 and 90% lower than that of 173 kg/mol PS, respectively. Such a transition is similar to previous observations by Wool et al. in bulk polystyrene samples.[49] The fracture energy of a PS film can be composed of the intrinsic fracture energy caused by chain pull-out and plastic energy dissipation caused by chain disentanglement and chain scission.[49,55] Owing to the high number of entanglements per chain (M_n/M_e) in high molecular weight PS, the amount of plastic energy dissipation upon disentanglement is more pronounced than that of low molecular weight PS (e.g., 51 kg/mol). The reduction in fracture energy indicates a transition of ductile-to-brittle failure behavior as the molecular weight of ultrathin PS films decreases. As seen in the optical images, the notch tip for 173 kg/mol got wider and blunted under displacement, followed by crack propagation. Conversely, 51 and 62 kg/mol PS display brittle failure instantly after the limited stress accumulation (Figure 4d and Figures S7 and S8). This observation demonstrates the vital role of interchain entanglement in enhancing the fracture energy of polymer ultrathin films.

2.5. Fracture Energy Measurement through Pure Shear Tests

When plastic energy dissipation has a substantial contribution to the total fracture energy, the total fracture energy is supposed to rise as the crack extends until reaching a steady-state value.[56] To confirm our observation of the brittle-to-ductile transition of PS ultrathin films with the molecular weight, we also conducted pure shear tests on both 51 and 173 kg/mol PS to obtain the steady-state fracture energies (Figure 4e,f and Figure S14). The ultrathin films were also laser-patterned into a rectangular shape with a thickness (t) of 80 nm, width (W) of 16 mm, and a length (L) of 2 mm, corresponding to a width-to-length ratio of 8 (Figure 4e). For each polymer, the force−displacement curves were measured for both an unnotched sample and a notched sample with a precrack half of the length of the sample. The measured steady-state fracture energy G_{ss} can be obtained by

$$G_{ss} = \frac{U(D_c)}{Wt} \tag{3}$$

where $U(D_c)$ is the elastic energy of the unnotched sample at the critical displacement D_c between the two grips when the stable notch turns into a running crack and can be calculated by the area underneath the force−displacement curve of the unnotched sample.[44,57] For 51 kg/mol PS, the critical displacement can be easily identified due to its brittle fracture behavior, and the fracture energy was determined to be around 95 J/m^2, similar to that measured from the Begley−Landes method, which indicates a negligible contribution of plastic dissipation to the total fracture energy. For 173 kg/mol PS, the fracture energy based on the measurement of the onset displacement for crack propagation, D_{onset}, is 1744 J/m^2. Unfortunately, before reaching the stable crack propagation condition, the stress concentration in the gripping region triggers an additional crack (Movie S2), which makes it challenging to accurately measure the fracture energy of 173 kg/mol PS. However, even the underestimated steady-state fracture energy value is much higher than that from the Begley−Landes method, indicating the significant contribution of plastic deformation to the total fracture energy, which leads to the brittle-to-ductile transition.

2.6. Finite Element Simulations

Further fracture analysis of PS films was performed through the cohesive zone model in finite element simulations (see Methods section for details). The intrinsic fracture energy for the cohesive elements for both the 51 and 173 kg/mol PS films was prescribed as 100 J/m^2, which is equal to the averaged total fracture energy measured for the 51 kg/mol PS at different thicknesses, as shown later in Figure 6c. Since the molecular weights of both are much higher than the entanglement molecular weight of 18 kg/mol, the intrinsic fracture energies are not expected to differ. In contrast to the 173 kg/mol PS, the 51 kg/mol PS was modeled as a linearly elastic material with the same modulus and Poisson's ratio as those of the 173 kg/mol PS. The simulated force−displacement curves of an 8 mm × 2 mm sample with a 0.6 mm notch length (the same dimension as that in the experiment) for both 173 and 51 kg/mol PS agree well with the experimental measurements (Figure 5a). The 173 kg/mol PS exhibits ductile fracture, indicated by the blunting of the crack tip with a large plastic zone size developed before the crack propagates, which results in a peak force as high as around 8 mN. The similar crack tip blunting was also observed in the experiment (Figure 2 and Figures S10−S12). In contrast, the 51 kg/mol PS exhibits brittle fracture without plasticity as an energy dissipation mechanism. As a result, the crack propagates immediately once the intrinsic fracture energy is achieved, resulting in a low peak force around 1.5 mN.

To determine the fracture resistance curves (R curve), that is, fracture energy as a function of crack extension, for the 173 and 51 kg/mol PS, their mode I crack growth under the plane stress condition was simulated subject to the small-scale yielding condition.[56] We modeled a large K-field zone of radius 20 mm, where the x-axis aligns along the crack plane, and the origin is positioned at the initial crack tip (Figure 5b). We selected the radius of the K-field zone to be 20 mm to guarantee it is much larger than the initial plastic zone size estimated by $R_0 = E_0/\pi\sigma_Y^2$ = 0.0134 mm, and the developing plastic zone size even after considerable crack propagation as the external loading increases. The displacement field, in accordance with linear elastic fracture mechanics, was prescribed on the outer circular boundary of the K-field zone

$$u_x = \frac{2K_I(1+\nu)}{E}\sqrt{\frac{r}{2\pi}}\cos\left(\frac{\theta}{2}\right)\left[\frac{1-\nu}{1+\nu} + \sin^2\left(\frac{\theta}{2}\right)\right]$$
$$u_y = \frac{2K_I(1+\nu)}{E}\sqrt{\frac{r}{2\pi}}\sin\left(\frac{\theta}{2}\right)\left[\frac{1-\nu}{1+\nu} + \cos^2\left(\frac{\theta}{2}\right)\right] \tag{4}$$

where r and θ are the radial and circumferential coordinates and K_I is the stress intensity factor, governing the amplitude of

https://doi.org/10.1021/acspolymersau.1c00005
ACS Polym. Au 2021, 1, 16−29

the displacement. The energy release rate G is directly calculated using the following equation:

$$G = \frac{K_I^2}{E} \tag{5}$$

The relation of G and the crack extension Δa is recorded as the R curve.

As the applied displacement field increases, the plastic zone develops at the crack tip for the 173 kg/mol PS. When G reaches 100 J/m^2, the first cohesive element reaches the maximum separation distance δ_{max} (Figure S3b), and the plastic zone size is 0.0134 mm, which is consistent with R_0 (Figure 5c). As G increases, the plastic zone size expands, and the crack tip blunts (Figure 5c), consistent with the experimental observation (Figures S2 and S10−S12). The crack does not propagate until G reaches a much higher value 3600 J/m^2, that is, $G/\Gamma_0 = 36$ (Figure 5d), which corresponds to the fracture energy experimentally measured by the Begley−Landes method. As G further increases, the crack extends downstream, and the material points in the plastic zone unload. Finally, the steady-state condition is reached where the stress field behind the advancing crack tip is invariant (Figure 5c,d). The steady-state fracture energy for the 173 kg/mol PS from the simulation is 4089 J/m^2, more than 40 times its intrinsic fracture energy. Correspondingly, the plastic zone size is 40 times larger than the initial size but still remains much smaller than the radius of the K-field zone. The significant increase of the total fracture energy compared to the intrinsic fracture energy originates from the plastic dissipation of the material when the plastic zone is unloaded as the crack propagates downstream. We also studied the effect of stretching limit parameter J_m on the fracture behavior. As J_m increases, the fracture energy increases as the less stiffened polymer induces a larger plastic zone size (Figure S15a). On the other hand, the maximum force that the notched sample discussed in Figure 5a can sustain before the notch catastrophically propagates decreases as J_m decreases (Figure S15b). Therefore, we chose $J_m = 200$ to better fit the simulation results to the experimental measurements. In contrast, the R curve for the 51 kg/mol PS is a horizontal line of value $G = 100$ J/m^2, indicating the steady-state fracture energy is exactly equal to the intrinsic fracture energy without plastic dissipation. Unlike the 173 kg/mol PS, the crack does not blunt for the 51 kg/mol PS but catastrophically propagates once G reaches the intrinsic fracture energy.

To further confirm the steady-state fracture energy obtained from the simulated R curve by the K-field zone method, the pure shear test was simulated using the same cohesive zone elements with the same parameters (Movie S3 and Movie S4). We chose the length and width of the simulated pure shear test sample to be 4 and 40 mm, respectively. Similar to the experiment, one notched and one unnotched sample were stretched quasi-statically along the length direction under the clamp boundary condition. In the notched sample, a precrack of 20 mm was introduced, and cohesive elements were implemented ahead of the crack tip. For the 173 kg/mol PS, as the external displacement D increases, the stress in the sample increases, and the plastic zone develops at the crack tip (Figure 5e). Again, the crack tip blunts before the crack propagates. The external force normalized by the sample width F/W reaches the maximum at the critical displacement normalized by the sample length $D_c/L = 1.0246$, indicating the onset of unstable crack growth (Figure 5f). From the simulation of the unnotched sample, the normalized force−displacement relation is obtained (Figure 5f). Using eq 3, we obtain the steady-state fracture energy of the 173 kg/mol PS as 4042 J/m^2, which agrees well with that from the R curve based on the K-field zone method. Although the pure shear test can measure the steady-state fracture energy of samples undergoing large-scale yielding (Figure 5f), the sample dimension needs to be large enough so that the boundary effect does not interfere with the fracture behavior of the material. This is the reason why we selected the width and length of the sample to be larger than that of the experiments. The pure shear simulation of the sample with the same dimension as the experiment measures a lower steady-state fracture energy 2874 J/m^2 (Figure S16), which can be another reason that the experiment may underestimate the steady-state fracture energy. Nevertheless, the pure shear simulation of the 51 kg/mol PS resulted in 101 J/m^2, in which the steady-state fracture energy of linear elastic material recovers the intrinsic fracture energy.

2.7. Film Thickness Effect on Fracture Energy

Besides the effect of molecular weight, film thickness, consequently the degree of chain confinement, could also play a critical role in the fracture behavior of ultrathin films due to two mechanisms: polymer chains at the air−film interface have higher mobility than the bulk;[12,35] polymer films with a thickness below the end-to-end distance, R_{ee}, of the polymer chains could have less interchain entanglements and more intrachain entanglements (Figure 6a).[43,58−60] Previous works using the film-on-elastomer method have demonstrated the elastic moduli of ultrathin PS films are lower than those of the bulk, while the crack onset strains are higher for thinner films.[11,61] The microprojectile impact test shows lower penetration energies for thinner films.[25] However, a quantitative measurement for the ultra-thin-film fracture energy under different degrees of confinement has not been reported in the literature. In this study, we measure the fracture energies of the 173 and 51 kg/mol PS representing ductile and brittle systems, respectively, of various thicknesses (Figure 6b−d and Figures S17−S25). For the 173 kg/mol PS, as the film thickness decreases, the fracture energy drops from around 1000 J/m^2 at a thickness above 50 nm (unconfined), to 538 J/m^2 at 36 nm and 276 J/m^2 at 26 nm (confined), corresponding to a 75% reduction. This trend results from the loss of interchain entanglements, leading to more chain pull-out and early onset of crack propagation.[43] Meanwhile, a lower elastic modulus at 26 nm is obtained at below R_{ee} due to the low T_g nature of the surface mobile layer. However, due to the low R_{ee} of 15 nm and lack of interchain entanglements, the 51 kg/mol PS shows near-constant elastic modulus and fracture energy of around 100 J/m^2 for films with a thickness from 40 to 120 nm. A much thinner PS film was not tested due to the challenge in transferring a brittle notched sample onto a water surface. Here, we observe the effect of confinement on facture behavior of ultrathin films. Interestingly, it is also noticed that a 26 nm confined 173 kg/mol PS film still exhibits a fracture energy roughly 3 times that of a 120 nm unconfined 51 kg/mol PS film, which suggests the significant role of polymer chain length in producing energy dissipation.

2.8. Fracture Energy Measurement of Semicrystalline Polymers

In addition to the model PS system, the same technique was employed to measure the fracture energies of functional

https://doi.org/10.1021/acspolymersau.1c00005
ACS Polym. Au 2021, 1, 16−29

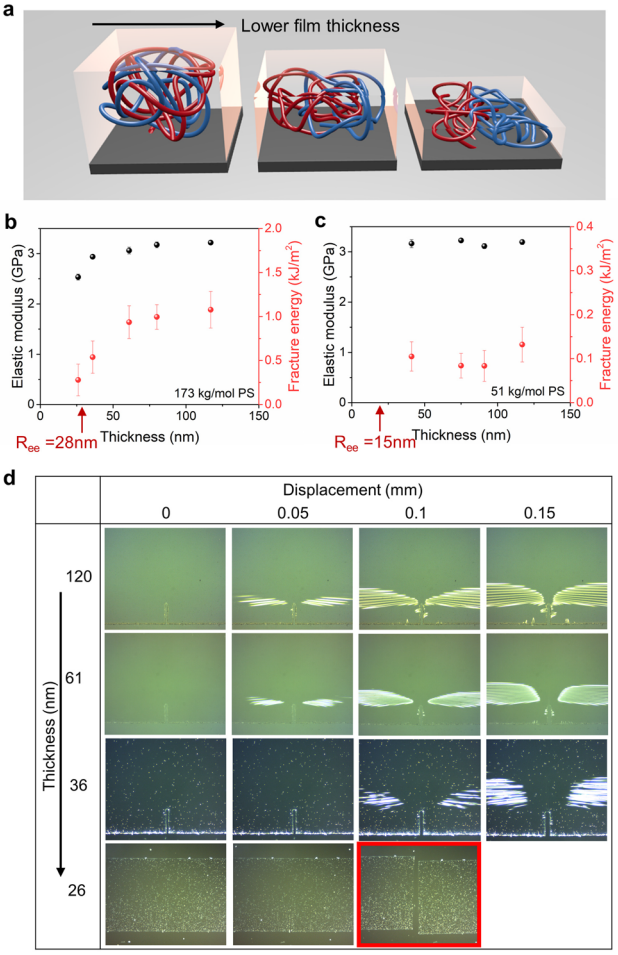

Figure 6. Effect of film thickness on the fracture behavior of PS ultrathin films. (a) Schematic showing the confinement effect on the number of chain entanglements under the same molecular weight. As the thickness decreases, the number of interchain entanglements decreases while the number of intrachain entanglements increases. (b,c) Elastic modulus (black) and fracture energy (red) versus thickness for (b) 173 kg/mol and (c) 51 kg/mol PS. (d) Optical images of 173 kg/mol PS films with 0.4 mm notch length and various film thicknesses at different displacements. The image with a red frame represents a fractured film.

semicrystalline polymers that are widely used in thin-film electronic devices to gain insights into their fracture behavior. Here, two semiconducting polymers are chosen, PNDI(2HD)-T and P3HT, due to their high potential in fabricating future flexible electronic devices. Previous research mainly focused on their thermal and mechanical properties, such as elastic moduli and crack-onset strains, but their fracture energies are still unknown.[31,62−68] As a result, PNDI(2HD)T exhibits a high T_g of 115 °C and a high elastic modulus of 890 MPa, whereas the fracture energy is determined to be 320 J/m^2 (Figure 7a−c and Figures S26 and S27). Upon deformation, the wrinkling pattern slowly builds up around the notch at an external displacement of 0.1 mm, followed by plastic failure without forming an SDZ. These wrinkling patterns slowly disappear with time, even under a fixed displacement due to the viscoelastic nature of PNDI(2HD)T (Movie S5). On the other hand, P3HT with a T_g of 25 °C and a lower elastic modulus of 315 MPa shows a much lower fracture energy of 78 J/m^2 (Figure 7d−f and Figure S28), compared to the other two polymers in this study. Furthermore, no obvious wrinkles are observed on P3HT thin films, indicating its highly mobile nature at room temperature (Figure 7e). The disparity between two polymer's fracture energies and wrinkling behavior likely results from the lower glass transition temperature and the lower molecular weight of P3HT compared to those of PNDI(2HD)T. It is noted that the fracture energy tested here is higher than that previously reported by the four-point bending test and double-cantilever beam test (<10 J/m^2).[31,69−72] Several reasons could contribute to such a difference. First, spin-coated thin films can be highly anisotropic along the thickness direction versus in-plane direction, and the measured fracture energies can be significantly different. The crack planes in the Begley−Landes method used in this paper and the four-point bending test are perpendicular to the in-plane direction, but the former propagates in the plane and the later propagates along the thickness.[73] In contrast, the crack plane in the double-cantilever beam test is parallel to the in-plane direction and propagates in the plane, which is expected to correspond to a lower fracture toughness. Second, when the crack propagates in the thickness direction in the four-point bending test, the plastic zone size is constrained by the film thickness, as previously observed in poly(arylene) ether, whereas the plastic zone size is not limited in the Begley−Landes method.[69] Therefore, the fracture energy measured by the four-point bending test can be much lower than that of the Begley−Landes method. Third, the fracture energy of viscoelastic semiconducting polymers can be rate-dependent. The loading rate in the Begley−Landes method in this paper (4 μm/s) is higher than that of the other two methods in the literature (0.5−0.8 μm/s) and can lead to a higher fracture energy. Our study presents the first direct measured fracture energies of semiconducting polymer thin films.

In this work, we demonstrate a new technique to measure the fracture energies of ultrathin films in a confined state. The proposed technique has been demonstrated in both amorphous and semicrystalline polymer systems. A ductile-to-brittle transition is observed in PS ultrathin films when either the molecular weight or film thickness decreases. From an experimental Begley−Landes method, the fracture energy shows a reduction from 1000 J/m^2 for 173 kg/mol PS to 100 J/m^2 for 51 kg/mol PS. Meanwhile, under the same molecular weight of 173 kg/mol, the fracture energy reduces by 75% as thickness decreases from 61 to 26 nm. Direct visualization of the stress field distribution, quantitative measurements of the fracture energy, and predictive finite element fracture simulations of the R curve provides us the understanding that plastic dissipation due to chain reorientation and disentanglement accounts for the significant increase of the total fracture energy compared to the intrinsic fracture energy. Besides its promising applications in polymeric thin films, this method can also be widely used in other fields and serve as a new platform to study fracture mechanics of inorganic or metallic thin films and emerging 2D materials at the device-relevant thickness range.

3. METHODS

3.1. Materials

All polymers (polystyrene (PS), poly{[*N*,*N*′-bis(2-hexylldecyl)-naphthalene-1,4,5,8-bis(dicarboximide)-2,6-diyl]-*alt*-2,5-thiophene} (PNDI(2HD)T), and poly(3-hexylthiophene) (P3HT)) and solvents (toluene, chlorobenzene) were purchased from commercial sources and used as received. The number-average molecular weight and the

https://doi.org/10.1021/acspolymersau.1c00005
ACS Polym. Au 2021, 1, 16−29

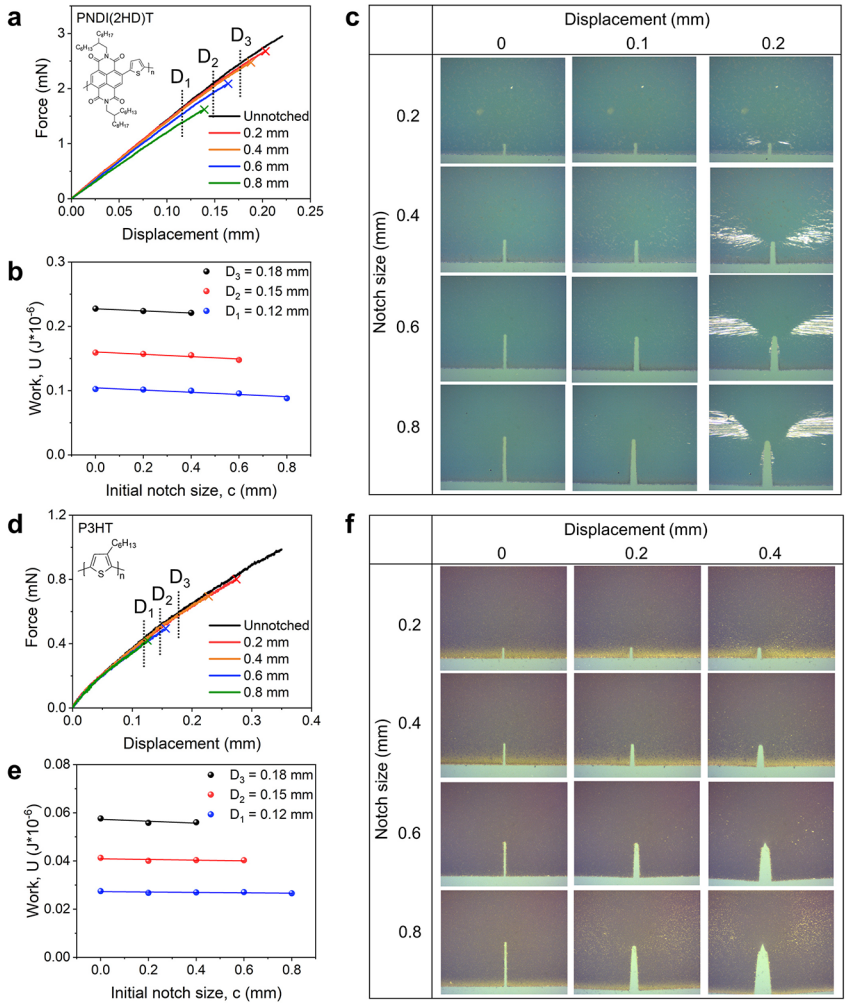

Figure 7. Fracture energy measurements for semicrystalline PNDI(2HD)T (58 nm) and P3HT (51 nm) polymers. (a,d) Force−displacement curves for dog-bone (a) PNDI(2HD)T and (d) P3HT samples with various notch sizes. (b,e) Work done as a function of notch size for the (b) PNDI(2HD)T and (e) P3HT thin films. (c,f) Optical images of polymer ultrathin films with various notch sizes at different displacements for (c) PNDI(2HD)T and (f) P3HT.

dispersity ($Đ$) of PS were evaluated by a gel-permeation chromatography (GPC) system consisting of a Waters Alliance 2695 separations module, an online multiangle laser light scattering (MALLS) detector fitted with a gallium arsenide laser (power: 20 mW) operating at 658 nm (miniDAWN TREOS, Wyatt Technology Inc.), an interferometric refractometer (Optilab rEX, Wyatt Technology Inc.) operating at 35 °C and 685 nm, and two PLgel (Polymer Laboratories Inc.) and mixed E columns (pore size range 50−103 Å, 3 μm bead size). Freshly distilled tetrahydrofuran (THF) served as the mobile phase and was delivered at a flow rate of 1.0 mL min^{-1}. The M_n and PDI of PNDI(2HD)T and P3HT were measured by high-temperature GPC using trichlorobenzene as the eluent at 160 °C, polystyrene for calibration, a viscometer, and light scattering as the detectors. Poly(sodium 4-styrenesulfonate) (PSS) was purchased from Sigma-Aldrich and used as received. Polydimethylsiloxane (PDMS) was purchased from Corning and used as received. PDMS stab was prepared by mixing the base and curing agent at a ratio of 10:1.

3.2. Fabrication of Bilayer Thin Films

PSS was dissolved in deionized (DI) water at a concentration of 3 mg/mL. Polystyrene was dissolved in toluene with a concentration ranging from 5 to 20 mg/mL. PNDI(2HD)T and P3HT were dissolved in chlorobenzene at a concentration of 10 mg/mL. The PSS solution was first spin-coated on top of a 6 × 6 cm silicon wafer at the speed of 4000 rpm for 1 min to form a 30 nm thick layer film. Next, the target polymer solution was spin-coated on top of the PSS layer at a speed of 2000 rpm for 2 min to form a composite film. The film thickness was later measured by AFM.

3.3. Thin-Film Fracture Energy Test with Begley−Landes Method

The polymer films were etched by an ultrafast laser cutter to pattern into a dog-bone shape on a silicon wafer, followed by patterning five different sizes of notches (0, 0.2, 0.4, 0.6, 0.8 mm) (Figure S1). Three samples of each notch size were prepared. Thin-film tensile tests were performed by a homemade pseudo-free-standing tensile tester. Details about the tensile stage setup can be found in our previous publication.[18] The force−displacement curve for an unnotched sample was first recorded during the tensile test at a strain rate of 5 × 10^{-4} s^{-1}, followed by converting it to a nominal stress−strain curve. The elastic modulus was obtained from the slope of the stress−strain curve using the first 0.5% strain. All samples with various notch sizes were separately tested and monitored with a high-resolution camera. The force−displacement curves were recorded until the onset of crack propagation. The total work is done to the sample; that is, the area underneath each curve was calculated and plotted versus the initial notch length under a fixed displacement, where the fracture energy was derived from the slope.

https://doi.org/10.1021/acspolymersau.1c00005
ACS Polym. Au 2021, 1, 16−29

3.4. Thin-Film Fracture Energy Test with the Pure Shear Method

The polymer film was laser-etched into an I shape with a 2 mm × 16 mm rectangular gauge, and two 2 mm × 20 mm rectangular pads. For a notched sample, an 8 mm long notch was introduced to its center along the width direction. The tensile test for all samples was performed at a strain rate of 5×10^{-3} s^{-1}. The critical displacement for stable crack propagation was identified from the force–displacement curve of notched samples.

3.5. Shear Rheometry Test

The linear viscoelastic response of 173 kg/mol PS was obtained from small amplitude oscillatory shear measurements performed on an ARES-LS rheometer (TA Instruments) using 8 mm aluminum disposal parallel plates. A PS sample was prepared to form a disk shape by compression molding under vacuum at 150 °C. The sample was loaded between the parallel plates and heated to 170 °C within a nitrogen-purged oven. Frequency sweep measurements were carried out over a temperature range of 170 to 120 °C with −10 °C increment, and the applied strain was in the linear range. The frequency range for the dynamic measurements was 100 to 0.1 rad/s.

3.6. Differential Scanning Calorimetry (DSC)

DSC measurement was performed on Mettler-Toledo DSC 3+ equipped with FRS6+ sensor under dry nitrogen gas purge with a flow rate of 50 mL/min. To remove the thermal history, a heat–cool–heat cycle with a heating/cooling rate of 10 °C/min was utilized over a temperature range of 160 to 50 °C. The data analysis was performed on the reheating scan.

3.7. Dynamic Mechanical Analysis (DMA)

A TA Q800 instrument was used to perform DMA measurement. Polymer solutions (5 mg mL^{-1}) were made and then drop-casted on top of a glass fiber mesh to prepare the samples.[74] The temperature corresponding to the peak of tan δ was determined as the backbone glass transition temperature. In strain-controlled mode, temperature ramp experiments were performed at a temperature range of −110 to 150 °C and a heating rate of 3 °C min^{-1} with a fixed frequency of 1 Hz. The strain imposed was in the linear regime.

3.8. Finite Element Simulations

We simulated deformation and crack propagation in polymer thin films subjected to an external load under the plane stress condition using ABAQUS/Explicit finite element analysis. While the 51 kg/mol PS films were modeled as a linearly elastic material, the 173 kg/mol PS films were modeled as an elasto-plastic material using a J_2 flow theory and isotropic hardening with the Gent hardening law shown in eq 1. The elastic modulus for both PS was set as E = 3.01 GPa obtained by fitting to the linear regime of the experimental force–displacement curves (Figure 5a and Figure S3c), and the Poisson's ratio υ = 0.34. For the 173 kg/mol PS, the other parameters were set as G_p = 15 MPa according to the literature[34] and σ_Y = 84 MPa and J_m = 200 according to nonlinear regime of the experimental force–displacement curves. All films were modeled using the plane-stress four-node linear elements with reduced integration (CPS4R), while a cohesive layer with the four-node two-dimensional cohesive elements (COH2D) was inserted ahead of the crack tips in notched films to allow crack propagation (Figure S3a).

In order to model the fracture behavior of the 51 and 173 kg/mol PS, we selected a bilinear cohesive zone model governed by the maximum cohesive stress σ_c, maximum separation distance between the crack planes δ_{max}, and the intrinsic fracture energy Γ_0 (Figure S3b). The damage initiation of the cohesive elements follows the maximum cohesive stress criterion

$$\max\left\{\frac{t_n}{\sigma_c}, \frac{t_s}{\sigma_c}\right\} = 1 \tag{6}$$

where t_n and t_s represent the tensile normal traction and tangential traction, respectively, on the crack surface. When eq 6 is satisfied, the cohesive elements enter their softening phase, where the cohesive stress starts to linearly decrease (Figure S3b). Complete separation between the crack planes is achieved when the cohesive stress becomes zero. The maximum cohesive stress for the bilinear traction separation law was set as σ_c = 300 MPa, and the area under the traction separation law is the intrinsic fracture energy Γ_0 = 100 J/m^2. To ensure that the cohesive elements do not suffer from interpenetration between crack surfaces, we arbitrarily made the elastic stiffness of the cohesive elements as high as possible E_{ts} = 78750 GPa but small enough to prevent spurious oscillations of the tractions in a cohesive element.[75] To correctly capture the stress distribution inside the cohesive zone for accurate prediction of crack propagation, we refined our cohesive mesh until convergence was met. As a result, the length of each cohesive element is less than a tenth of the bridging zone size defined as $E\Gamma_0/\sigma_c^2$; that is, 16 cohesive elements are modeled within the bridging zone.

To obtain the force displacement curves of the notched samples (Figure 5a), displacement in the vertical direction was applied to the top edge of the film at a strain rate of 1%/s to ensure quasi-static crack analysis, while the other edge is only free to move in the horizontal direction. To obtain the R curves, displacement boundary conditions given in eq 5 were applied on the entire circumference of the circular K-field zone. The amplitude of the prescribed displacement fields in the both the x and the y directions was incrementally increased at a strain rate of 1%/s. For the pure shear simulations, the entire bottom edge was firmly clamped, whereas the entire top edge could only displace in the vertical direction at the same strain rate of 1%/s, and the side edges of the pure shear specimens are free surfaces. Since the stable time increment in explicit simulations depend on the velocity of the elastic wave traveling through the smallest elements, we used mass scaling up to 6 orders of magnitude to artificially reduce the elastic wave speed, thereby increasing the time increments for the simulations to finish in a reasonable time limit. Excessive mass scaling can result in inaccurate results due to inertia interfering with the quasi-static crack analysis. However, we confirmed that our mass scaling does not influence the results by verifying it with linear elastic crack analysis.

3.9. Transmission Electron Microscopy

The deformed thin film was characterized by TEM instruments from Low Activation Materials Design and Analysis Laboratory, Oak Ridge National Laboratory. Microstructure of the crack tip was analyzed with a JEOL JEM 2100F TEM operated at 200 kV. The voids were imaged in under-focused conditions.

■ ASSOCIATED CONTENT

Supporting Information

The Supporting Information is available free of charge at https://pubs.acs.org/doi/10.1021/acspolymersau.1c00005.

Supplementary Figures S1–S28 and Table S1 (PDF)

Movie S1: Begley–Landes method on 173 kg/mol PS ultrathin film (MOV)

Movie S2: Pure shear test on 173 kg/mol PS ultrathin film (MOV)

Movie S3: Simulated pure shear test on 173 kg/mol PS ultrathin film (MP4)

Movie S4: Simulated pure shear test on 51 kg/mol PS ultrathin film (MP4)

Movie S5: Relaxation of wrinkling for PNDI2HDT ultrathin film (MP4)

■ AUTHOR INFORMATION

Corresponding Authors

Lihua Jin − *Department of Mechanical and Aerospace Engineering, University of California, Los Angeles, Los Angeles, California 90095, United States*; Email: lihuajin@seas.ucla.edu

https://doi.org/10.1021/acspolymersau.1c00005
ACS Polym. Au 2021, 1, 16–29

Xiaodan Gu − *School of Polymer Science and Engineering, Center for Optoelectronic Materials and Device, The University of Southern Mississippi, Hattiesburg, Mississippi 39406, United States;* orcid.org/0000-0002-1123-3673; Email: xiaodan.gu@usm.edu

Authors

Song Zhang − *School of Polymer Science and Engineering, Center for Optoelectronic Materials and Device, The University of Southern Mississippi, Hattiesburg, Mississippi 39406, United States;* orcid.org/0000-0001-9815-7046

Masato Koizumi − *Department of Mechanical and Aerospace Engineering, University of California, Los Angeles, Los Angeles, California 90095, United States*

Zhiqiang Cao − *School of Polymer Science and Engineering, Center for Optoelectronic Materials and Device, The University of Southern Mississippi, Hattiesburg, Mississippi 39406, United States*

Keyou S. Mao − *Materials Science and Technology Division, Oak Ridge National Laboratory, Oak Ridge, Tennessee 37831, United States*

Zhiyuan Qian − *School of Polymer Science and Engineering, Center for Optoelectronic Materials and Device, The University of Southern Mississippi, Hattiesburg, Mississippi 39406, United States;* orcid.org/0000-0002-7674-057X

Luke A. Galuska − *School of Polymer Science and Engineering, Center for Optoelectronic Materials and Device, The University of Southern Mississippi, Hattiesburg, Mississippi 39406, United States*

Complete contact information is available at: https://pubs.acs.org/10.1021/acspolymersau.1c00005

Author Contributions

S.Z. and M.K. contributed equally to this work. X.G. and L.J. conceived the concept of this paper and designed and directed the project. S.Z. performed thin-film tensile tests and AFM measurements. M.K. performed the ABAQUS simulation study. Z.Q. performed rheology and DSC measurement. Z.C. performed the DMA test. K.S.M. performed the TEM test. L.A.G. performed free-standing tensile tests. S.Z., M.K., L.J., and X.G. wrote the initial draft of manuscript. All authors have given approval to the final version of the manuscript.

Funding

This work is supported by the USM's faculty start up and the National Science Foundation through Grant No. DMR-2047689. S.Z., Z.C., and X.G. also acknowledge the partial support from the National Science Foundation through Grant No. OIA-1757220. M.K. and L.J. acknowledge the support from the National Science Foundation through Grant No. CMMI-1925790. L.A.G. acknowledges support from the NSF NRT program "Interface" award #DGE-1449999) through the University of Southern Mississippi.

Notes

The authors declare no competing financial interest.

■ ACKNOWLEDGMENTS

The authors acknowledge Prof. John Hutchinson of Harvard University for fruitful discussions on the elasto-plastic fracture simulations. The authors also thank the Dr. Robson Storey and Jason Azoulay group at USM for accessing GPC for molecular weight characterization. This work used computational and storage services associated with the Hoffman2 Shared Cluster provided by Institute for Digital Research and Education's Research Technology Group at the University of California, Los Angeles. A portion of this research was conducted at the Center for Nanophase Materials Sciences, which is a DOE Office of Science User Facility.

■ REFERENCES

(1) Ismail, A. F.; Padaki, M.; Hilal, N.; Matsuura, T.; Lau, W. J. Thin Film Composite Membrane — Recent Development and Future Potential. *Desalination* **2015**, *356*, 140−148.

(2) Jeong, B.-H.; Hoek, E. M. V.; Yan, Y.; Subramani, A.; Huang, X.; Hurwitz, G.; Ghosh, A. K.; Jawor, A. Interfacial Polymerization of Thin Film Nanocomposites: A New Concept for Reverse Osmosis Membranes. *J. Membr. Sci.* **2007**, *294* (1−2), 1−7.

(3) Yip, N. Y.; Tiraferri, A.; Phillip, W. A.; Schiffman, J. D.; Elimelech, M. High Performance Thin-Film Composite Forward Osmosis Membrane. *Environ. Sci. Technol.* **2010**, *44* (10), 3812−3818.

(4) Wang, S.; Xu, J.; Wang, W.; Wang, G. J. N.; Rastak, R.; Molina-Lopez, F.; Chung, J. W.; Niu, S.; Feig, V. R.; Lopez, J.; Lei, T.; Kwon, S. K.; Kim, Y.; Foudeh, A. M.; Ehrlich, A.; Gasperini, A.; Yun, Y.; Murmann, B.; Tok, J. B. H.; Bao, Z. Skin Electronics from Scalable Fabrication of an Intrinsically Stretchable Transistor Array. *Nature* **2018**, *555* (7694), 83−88.

(5) Xu, J.; Wu, H. C.; Zhu, C.; Ehrlich, A.; Shaw, L.; Nikolka, M.; Wang, S.; Molina-Lopez, F.; Gu, X.; Luo, S.; Zhou, D.; Kim, Y. H.; Wang, G. J. N.; Gu, K.; Feig, V. R.; Chen, S.; Kim, Y.; Katsumata, T.; Zheng, Y. Q.; Yan, H.; Chung, J. W.; Lopez, J.; Murmann, B.; Bao, Z. Multi-Scale Ordering in Highly Stretchable Polymer Semiconducting Films. *Nat. Mater.* **2019**, *18* (6), 594−601.

(6) Oh, J. Y.; Bao, Z. Second Skin Enabled by Advanced Electronics. *Adv. Sci.* **2019**, *6* (11), 1900186.

(7) Oh, J. Y.; Rondeau-Gagné, S.; Chiu, Y. C.; Chortos, A.; Lissel, F.; Wang, G. J. N.; Schroeder, B. C.; Kurosawa, T.; Lopez, J.; Katsumata, T.; Xu, J.; Zhu, C.; Gu, X.; Bae, W. G.; Kim, Y.; Jin, L.; Chung, J. W.; Tok, J. B. H.; Bao, Z. Intrinsically Stretchable and Healable Semiconducting Polymer for Organic Transistors. *Nature* **2016**, *539* (7629), 411−415.

(8) Xu, J.; Wang, S.; Wang, G.-J. N. J. N.; Zhu, C.; Luo, S.; Jin, L.; Gu, X.; Chen, S.; Feig, V. R.; To, J. W. F. F.; Rondeau-Gagné, S.; Park, J.; Schroeder, B. C.; Lu, C.; Oh, J. Y.; Wang, Y.; Kim, Y.-H. H.; Yan, H.; Sinclair, R.; Zhou, D.; Xue, G.; Murmann, B.; Linder, C.; Cai, W.; Tok, J. B. H.; Chung, J. W.; Bao, Z. Highly Stretchable Polymer Semiconductor Films through the Nanoconfinement Effect. *Science* **2017**, *355* (6320), 59−64.

(9) Gu, X.; Shaw, L.; Gu, K.; Toney, M. F.; Bao, Z. The Meniscus-Guided Deposition of Semiconducting Polymers. *Nat. Commun.* **2018**, *9* (1), 534.

(10) Stafford, C. M.; Harrison, C.; Beers, K. L.; Karim, A.; Amis, E. J.; Vanlandingham, M. R.; Kim, H. C.; Volksen, W.; Miller, R. D.; Simonyi, E. E. A Buckling-Based Metrology for Measuring the Elastic Moduli of Polymeric Thin Films. *Nat. Mater.* **2004**, *3* (8), 545−550.

(11) Stafford, C. M.; Vogt, B. D.; Harrison, C.; Julthongpiput, D.; Huang, R. Elastic Moduli of Ultrathin Amorphous Polymer Films. *Macromolecules* **2006**, *39* (15), 5095−5099.

(12) Forrest, J. A.; Dalnoki-Veress, K.; Dutcher, J. R. Interface and Chain Confinement Effects on the Glass Transition Temperature of Thin Polymer Films. *Phys. Rev. E: Stat. Phys., Plasmas, Fluids, Relat. Interdiscip. Top.* **1997**, *56* (5), 5705−5716.

(13) Hanakata, P. Z.; Pazmiño Betancourt, B. A.; Douglas, J. F.; Starr, F. W. A Unifying Framework to Quantify the Effects of Substrate Interactions, Stiffness, and Roughness on the Dynamics of Thin Supported Polymer Films. *J. Chem. Phys.* **2015**, *142* (23), 234907.

(14) Yang, Z.; Fujii, Y.; Lee, F. K.; Lam, C. H.; Tsui, O. K. C. Glass Transition Dynamics and Surface Layer Mobility in Unentangled Polystyrene Films. *Science* **2010**, *328* (5986), 1676−1679.

(15) Russell, T. P.; Chai, Y. 50th Anniversary Perspective: Putting the Squeeze on Polymers: A Perspective on Polymer Thin Films and Interfaces. *Macromolecules* **2017**, *50* (12), 4597−4609.
(16) Torres, J. M.; Stafford, C. M.; Vogt, B. D. Impact of Molecular Mass on the Elastic Modulus of Thin Polystyrene Films. *Polymer* **2010**, *51* (18), 4211−4217.
(17) Kim, J.-H.; Nizami, A.; Hwangbo, Y.; Jang, B.; Lee, H.-J.; Woo, C.-S.; Hyun, S.; Kim, T.-S. Tensile Testing of Ultra-Thin Films on Water Surface. *Nat. Commun.* **2013**, *4* (1), 2520.
(18) Zhang, S.; Ocheje, M. U.; Luo, S.; Ehlenberg, D.; Appleby, B.; Weller, D.; Zhou, D.; Rondeau-Gagné, S.; Gu, X. Probing the Viscoelastic Property of Pseudo Free-Standing Conjugated Polymeric Thin Films. *Macromol. Rapid Commun.* **2018**, *39* (14), 1800092.
(19) Liu, Y.; Chen, Y. C.; Hutchens, S.; Lawrence, J.; Emrick, T.; Crosby, A. J. SI-Directly Measuring the Complete Stress-Strain Response of Ultrathin Polymer Films. *Macromolecules* **2015**, *48* (18), 6534−6540.
(20) Bay, R. K.; Shimomura, S.; Liu, Y.; Ilton, M.; Crosby, A. J. Confinement Effect on Strain Localizations in Glassy Polymer Films. *Macromolecules* **2018**, *51* (10), 3647−3653.
(21) Bay, R. K.; Crosby, A. J. Uniaxial Extension of Ultrathin Freestanding Polymer Films. *ACS Macro Lett.* **2019**, *8* (9), 1080−1085.
(22) Galuska, L. A.; Muckley, E. S.; Cao, Z.; Ehlenberg, D. F.; Qian, Z.; Zhang, S.; Rondeau-Gagné, S.; Phan, M. D.; Ankner, J. F.; Ivanov, I. N.; Gu, X. SMART Transfer Method to Directly Compare the Mechanical Response of Water-Supported and Free-Standing Ultrathin Polymeric Films. *Nat. Commun.* **2021**, *12* (1), 2347.
(23) Murray, J.; Hull, D. Inherent Flaw Size and Fracture Energy of Polystyrene. *J. Mater. Sci.* **1971**, *6* (10), 1277−1285.
(24) DeVries, K. L.; Nuismer, R. J. Fracture Mechanics of Polymers. *ACS Symp. Ser.* **1985**, *17* (3), 277−304.
(25) Hyon, J.; Lawal, O.; Fried, O.; Thevamaran, R.; Yazdi, S.; Zhou, M.; Veysset, D.; Kooi, S. E.; Jiao, Y.; Hsiao, M. S.; Streit, J.; Vaia, R. A.; Thomas, E. L. Extreme Energy Absorption in Glassy Polymer Thin Films by Supersonic Micro-Projectile Impact. *Mater. Today* **2018**, *21* (8), 817−824.
(26) Lee, J.-H.; Loya, P. E.; Lou, J.; Thomas, E. L. Dynamic Mechanical Behavior of Multilayer Graphene via Supersonic Projectile Penetration. *Science* **2014**, *346* (6213), 1092−1096.
(27) Lee, J.-H.; Veysset, D.; Singer, J. P.; Retsch, M.; Saini, G.; Pezeril, T.; Nelson, K. A.; Thomas, E. L. High Strain Rate Deformation of Layered Nanocomposites. *Nat. Commun.* **2012**, *3* (1), 1164.
(28) Ma, Q.; Fujimoto, H.; Flinn, P.; Jain, V.; Adibi-Rizi, F.; Moghadam, F.; Dauskardt, R. H. Quantitative Measurement of Interface Fracture Energy in Multi-Layer Thin Film Structures. *Mater. Res. Soc. Symp. Proc.* **1995**, *391* (2), 91−96.
(29) Bruner, C.; Dauskardt, R. Role of Molecular Weight on the Mechanical Device Properties of Organic Polymer Solar Cells. *Macromolecules* **2014**, *47* (3), 1117−1121.
(30) Dupont, S. R.; Oliver, M.; Krebs, F. C.; Dauskardt, R. H. Interlayer Adhesion in Roll-to-Roll Processed Flexible Inverted Polymer Solar Cells. *Sol. Energy Mater. Sol. Cells* **2012**, *97*, 171−175.
(31) Balar, N.; O'Connor, B. T. Correlating Crack Onset Strain and Cohesive Fracture Energy in Polymer Semiconductor Films. *Macromolecules* **2017**, *50* (21), 8611−8618.
(32) Martinez, A. B.; Gamez-Perez, J.; Sanchez-Soto, M.; Velasco, J. I.; Santana, O. O.; Ll Maspoch, M. The Essential Work of Fracture (EWF) Method - Analyzing the Post-Yielding Fracture Mechanics of Polymers. *Eng. Failure Anal.* **2009**, *16* (8), 2604−2617.
(33) Prentice, P. Influence of Molecular Weight on the Fracture of Poly(Methyl Methacrylate) (PMMA). *Polymer* **1983**, *24* (3), 344−350.
(34) Nicholson, L. M.; Whitley, K. S.; Gates, T. S.; Hinkley, J. A. Influence of Molecular Weight on the Mechanical Performance of a Thermoplastic Glassy Polyimide. *J. Mater. Sci.* **2000**, *35* (24), 6111−6121.
(35) Forrest, J. A.; Dalnoki-Veress, K.; Stevens, J. R.; Dutcher, J. R. Effect of Free Surfaces on the Glass Transition Temperature of Thin Polymer Films. *Phys. Rev. Lett.* **1996**, *77* (10), 2002−2005.
(36) Jones, R. L.; Kumar, S. K.; Ho, D. L.; Briber, R. M.; Russell, T. P. Chain Conformation in Ultrathin Polymer Films. *Nature* **1999**, *400* (6740), 146−149.
(37) Zhang, S.; Ocheje, M. U.; Huang, L.; Galuska, L.; Cao, Z.; Luo, S.; Cheng, Y.; Ehlenberg, D.; Goodman, R. B.; Zhou, D.; Liu, Y.; Chiu, Y.; Azoulay, J. D.; Rondeau-Gagné, S.; Gu, X. The Critical Role of Electron-Donating Thiophene Groups on the Mechanical and Thermal Properties of Donor-Acceptor Semiconducting Polymers. *Adv. Electron. Mater.* **2019**, *5* (5), 1800899.
(38) Zhang, S.; Alesadi, A.; Selivanova, M.; Cao, Z.; Qian, Z.; Luo, S.; Galuska, L.; Teh, C.; Ocheje, M. U.; Mason, G. T.; St. Onge, P. B. J.; Zhou, D.; Rondeau-Gagne, S.; Xia, W.; Gu, X. Toward the Prediction and Control of Glass Transition Temperature for Donor-Acceptor Polymers. *Adv. Funct. Mater.* **2020**, *30* (27), 2002221.
(39) Zhang, S.; Cheng, Y.; Galuska, L.; Roy, A.; Lorenz, M.; Chen, B.; Luo, S.; Li, Y.; Hung, C.; Qian, Z.; St. Onge, P. B. J.; Mason, G. T.; Cowen, L.; Zhou, D.; Nazarenko, S. I.; Storey, R. F.; Schroeder, B. C.; Rondeau-Gagné, S.; Chiu, Y.; Gu, X. Tacky Elastomers to Enable Tear-Resistant and Autonomous Self-Healing Semiconductor Composites. *Adv. Funct. Mater.* **2020**, *30* (27), 2000663.
(40) Cerda, E.; Ravi-Chandar, K.; Mahadevan, L. Thin Films: Wrinkling of an Elastic Sheet under Tension. *Nature* **2002**, *419* (6907), 579−580.
(41) Haward, R. N. The Derivation of a Strain Hardening Modulus from True Stress-Strain Curves for Thermoplastics. *Polymer* **1994**, *35* (18), 3858−3862.
(42) Vorselaars, B.; Lyulin, A. V.; Michels, M. A. J. Microscopic Mechanisms of Strain Hardening in Glassy Polymers. *Macromolecules* **2009**, *42* (15), 5829−5842.
(43) Si, L.; Massa, M. V.; Dalnoki-Veress, K.; Brown, H. R.; Jones, R. A. L. Chain Entanglement in Thin Freestanding Polymer Films. *Phys. Rev. Lett.* **2005**, *94* (12), 127801.
(44) Rivlin, R. S.; Thomas, A. G. Rupture of Rubber. I. Characteristic Energy for Tearing. *J. Polym. Sci.* **1953**, *10* (3), 291−318.
(45) Begley, J. A.; Landes, J. D. The J Integral as a Fracture Criterion. *Fracture Toughness: Part II*; ASTM International, 1972.
(46) Berry, J. P. Fracture Processes in Polymeric Materials. II. The Tensile Strength of Polystyrene. *J. Polym. Sci.* **1961**, *50* (154), 313−321.
(47) Marshall, G. P.; Culver, L. E.; Williams, J. G. Fracture Phenomena in Polystyrene. *Int. J. Fract.* **1973**, *9* (3), 295−309.
(48) Kusy, R. P.; Katz, M. J. Generalized Theory of the Total Fracture Surface Energy for Glassy Organic Polymers. *Polymer* **1978**, *19* (11), 1345−1357.
(49) Wool, R. P. Rigidity Percolation Model of Polymer Fracture. *J. Polym. Sci., Part B: Polym. Phys.* **2005**, *43* (2), 168−183.
(50) Adolf, D.; Tirrell, M.; Prager, S. Molecular Weight Dependence of Healing and Brittle Fracture in Amorphous Polymers Above the Entanglement Molecular Weight. *J. Polym. Sci., Polym. Phys. Ed.* **1985**, *23* (2), 413−427.
(51) Hui, C. Y.; Kramer, E. J. Molecular Weight Dependence of the Fracture Toughness of Glassy Polymers Arising from Crack Propagation through a Craze. *Polym. Eng. Sci.* **1995**, *35* (5), 419−425.
(52) Kusy, R. P.; Turner, D. T. Influence of the Molecular Weight of Poly (Methyl Methacrylate) on Fracture Morphology in Notched Tension. *Polymer* **1977**, *18*, 391−402.
(53) Ferry, J. D. *Viscoelastic Properties of Polymers*; John Wiley & Sons, Ltd.: New York, 1980.
(54) Fox, T. G.; Flory, P. J. Second-Order Transition Temperatures and Related Properties of Polystyrene. I. Influence of Molecular Weight. *J. Appl. Phys.* **1950**, *21* (6), 581−591.
(55) Sambasivam, M.; Klein, A.; Sperling, L. H. The Molecular Basis of Fracture in Polystyrene Films: Role of Molecular Weight. *J. Appl. Polym. Sci.* **1995**, *58* (2), 357−366.

https://doi.org/10.1021/acspolymersau.1c00005
ACS Polym. Au 2021, 1, 16−29

(56) Tvergaard, V.; Hutchinson, J. W. The Relation between Crack Growth Resistance and Fracture Process Parameters in Elastic-Plastic Solids. *J. Mech. Phys. Solids* **1992**, *40* (6), 1377−1397.
(57) Sun, J. Y.; Zhao, X.; Illeperuma, W. R. K.; Chaudhuri, O.; Oh, K. H.; Mooney, D. J.; Vlassak, J. J.; Suo, Z. Highly Stretchable and Tough Hydrogels. *Nature* **2012**, *489* (7414), 133−136.
(58) García, N. A.; Barrat, J. L. Entanglement Reduction Induced by Geometrical Confinement in Polymer Thin Films. *Macromolecules* **2018**, *51* (23), 9850−9860.
(59) Zhang, T.; Winey, K. I.; Riggleman, R. A. Polymer Conformations and Dynamics under Confinement with Two Length Scales. *Macromolecules* **2019**, *52* (1), 217−226.
(60) Pressly, J. F.; Riggleman, R. A.; Winey, K. I. Increased Polymer Diffusivity in Thin-Film Confinement. *Macromolecules* **2019**, *52* (16), 6116−6125.
(61) Lee, J.-H.; Chung, J. Y.; Stafford, C. M. Effect of Confinement on Stiffness and Fracture of Thin Amorphous Polymer Films. *ACS Macro Lett.* **2012**, *1* (1), 122−126.
(62) Sharma, A.; Pan, X.; Bjuggren, J. M.; Gedefaw, D.; Xu, X.; Kroon, R.; Wang, E.; Campbell, J. A.; Lewis, D. A.; Andersson, M. R. Probing the Relationship between Molecular Structures, Thermal Transitions, and Morphology in Polymer Semiconductors Using a Woven Glass-Mesh-Based DMTA Technique. *Chem. Mater.* **2019**, *31* (17), 6740−6749.
(63) Kim, T.; Kim, J. H.; Kang, T. E.; Lee, C.; Kang, H.; Shin, M.; Wang, C.; Ma, B.; Jeong, U.; Kim, T. S.; Kim, B. J. Flexible, Highly Efficient All-Polymer Solar Cells. *Nat. Commun.* **2015**, *6*, 8547.
(64) Alkhadra, M. A.; Root, S. E.; Hilby, K. M.; Rodriquez, D.; Sugiyama, F.; Lipomi, D. J. Quantifying the Fracture Behavior of Brittle and Ductile Thin Films of Semiconducting Polymers. *Chem. Mater.* **2017**, *29* (23), 10139−10149.
(65) Chen, A. X.; Kleinschmidt, A. T.; Choudhary, K.; Lipomi, D. J. Beyond Stretchability: Strength, Toughness, and Elastic Range in Semiconducting Polymers. *Chem. Mater.* **2020**, *32* (18), 7582−7601.
(66) Qian, Z.; Cao, Z.; Galuska, L.; Zhang, S.; Xu, J.; Gu, X. Glass Transition Phenomenon for Conjugated Polymers. *Macromol. Chem. Phys.* **2019**, *220* (11), 1900062.
(67) Rolston, N.; Bush, K. A.; Printz, A. D.; Gold-Parker, A.; Ding, Y.; Toney, M. F.; McGehee, M. D.; Dauskardt, R. H. Engineering Stress in Perovskite Solar Cells to Improve Stability. *Adv. Energy Mater.* **2018**, *8* (29), 1802139.
(68) Rolston, N.; Printz, A. D.; Tracy, J. M.; Weerasinghe, H. C.; Vak, D.; Haur, L. J.; Priyadarshi, A.; Mathews, N.; Slotcavage, D. J.; McGehee, M. D.; Kalan, R. E.; Zielinski, K.; Grimm, R. L.; Tsai, H.; Nie, W.; Mohite, A. D.; Gholipour, S.; Saliba, M.; Grätzel, M.; Dauskardt, R. H. Effect of Cation Composition on the Mechanical Stability of Perovskite Solar Cells. *Adv. Energy Mater.* **2018**, *8* (9), 1702116.
(69) Brand, V.; Bruner, C.; Dauskardt, R. H. Cohesion and Device Reliability in Organic Bulk Heterojunction Photovoltaic Cells. *Sol. Energy Mater. Sol. Cells* **2012**, *99*, 182−189.
(70) Tummala, N. R.; Bruner, C.; Risko, C.; Brédas, J. L.; Dauskardt, R. H. Molecular-Scale Understanding of Cohesion and Fracture in P3HT: Fullerene Blends. *ACS Appl. Mater. Interfaces* **2015**, *7* (18), 9957−9964.
(71) Tummala, N. R.; Risko, C.; Bruner, C.; Dauskardt, R. H.; Brédas, J. L. Entanglements in P3HT and Their Influence on Thin-Film Mechanical Properties: Insights from Molecular Dynamics Simulations. *J. Polym. Sci., Part B: Polym. Phys.* **2015**, *53* (13), 934−942.
(72) Kim, J. H.; Gadisa, A.; Schaefer, C.; Yao, H.; Gautam, B. R.; Balar, N.; Ghasemi, M.; Constantinou, I.; So, F.; O'Connor, B. T.; Gundogdu, K.; Hou, J.; Ade, H. Strong Polymer Molecular Weight-Dependent Material Interactions: Impact on the Formation of the Polymer/Fullerene Bulk Heterojunction Morphology. *J. Mater. Chem. A* **2017**, *5* (25), 13176−13188.
(73) Bruner, C.; Novoa, F.; Dupont, S.; Dauskardt, R. Decohesion Kinetics in Polymer Organic Solar Cells. *ACS Appl. Mater. Interfaces* **2014**, *6* (23), 21474−21483.
(74) Sharma, A.; Pan, X.; Campbell, J. A.; Andersson, M. R.; Lewis, D. A. Unravelling the Thermomechanical Properties of Bulk Heterojunction Blends in Polymer Solar Cells. *Macromolecules* **2017**, *50* (8), 3347−3354.
(75) Turon, A.; Dávila, C. G. G.; Camanho, P. P. P.; Costa, J. An Engineering Solution for Mesh Size Effects in the Simulation of Delamination Using Cohesive Zone Models. *Eng. Fract. Mech.* **2007**, *74* (10), 1665−1682.

https://doi.org/10.1021/acspolymersau.1c00005
ACS Polym. Au 2021, 1, 16−29